

## Textures and grain boundary character distributions in a cold rolled and annealed Pb–Ca based alloy

Weiguo Wang<sup>a,\*</sup>, Bangxin Zhou<sup>b</sup>, Gregory S. Rohrer<sup>c</sup>, Hong Guo<sup>a</sup>, Zhengxu Cai<sup>a</sup>

<sup>a</sup> School of Mechanical Engineering, Shandong University of Technology, No. 12, Zhangzhou Road, Zibo 255049, Shandong, PR China

<sup>b</sup> Institute of Materials, School of Materials Science and Engineering, Shanghai University, Shanghai 200072, PR China

<sup>c</sup> Department of Materials Science and Engineering, Carnegie Mellon University, Pittsburgh, PA 15213-3890, USA

### ARTICLE INFO

#### Article history:

Received 1 November 2009

Received in revised form 20 January 2010

Accepted 22 March 2010

#### Keywords:

Texture

Grain boundary character distribution

Pb–Ca-based alloy

Thermomechanical processing

### ABSTRACT

Samples of a Pb–0.08%Ca–1.8%Sn–0.026%Al alloy were cold rolled at  $-196^{\circ}\text{C}$  to a reduction in thickness of 10–60%, and then annealed for 3 min at  $270^{\circ}\text{C}$ . The textures after rolling and after annealing were measured using electron backscatter diffraction. The special boundary content of the final microstructures varied from 13% to 81%, with the minimum found in the sample with 10% strain and the maximum in the sample with 40% strain. The sample with the highest fraction of special boundaries also contains texture components, which were developed by the so-called oriented growth (OG) of Goss ( $\{110\}\{001\}$ ), R1 ( $\{124\}\{121\}$ ), R2 ( $\{114\}\{221\}$ ) and R3 ( $\{123\}\{301\}$ ) orientations (including their geometric variants). These texture components are related by the  $\sum 3^n$  ( $n = 1, 2, 3$ ) misorientations and this contributes to the high special boundary fraction.

© 2010 Elsevier B.V. All rights reserved.

### 1. Introduction

Pb–Ca-based alloys are currently used to make the anode grids of lead acid batteries. Although Pb–Ca-based alloys can overcome the drawbacks of conventional Pb–Sb-based alloys (including high electric resistance, frequent maintenance and undesirable exhaustion of toxic gas), their intergranular corrosion (IGC) resistance is no better. This is the main cause for the fairly short charge–discharge life-span of lead acid batteries. Palumbo et al. [1,2] were the first to show that the IGC resistance of Pb–Ca alloys could be improved by the application of so-called grain boundary engineering (GBE). The GBE concept, originally proposed by Watanabe [3], involves sequential thermomechanical processing to optimize the grain boundary character distribution (GBCD) for a specific property. Palumbo et al. [1,2] demonstrated that a GBE processed Pb–Ca–Sn–Ag alloy with a special grain boundary (SB) [4] length fraction (out of the total grain boundary length in two-dimensional measurement) of about 70% had twice the IGC resistance of the cast materials that are conventionally used. Lee et al. [5] reported SB fractions as high as 96% in a Pb–Ca–Sn alloy that was cold rolled to a 30% reduction in thickness and annealed for 15 min at  $270^{\circ}\text{C}$ . Nearly all of the boundaries were  $\Sigma 3$ ,  $\Sigma 9$ , and  $\Sigma 27$ , which made up 67%, 21%, and 8% of the boundary fraction. This suggests that the measurements were all collected within one large twin cluster.

The paper, however, does not report the size of the area examined or the number of boundaries that were considered [5].

GBE processing has also been studied for other important engineering materials such as austenitic stainless steels [6–10], nickel-based superalloys [11–14] and copper–zinc alloys (brass) [15,16]. Because these materials (including Pb–Ca-based alloys) are all low to medium stacking faults energy (SFE) fcc metals, thermomechanical processing results in the formation of many twins ( $\Sigma 3$  boundaries). The twins and twin related boundaries are the most common type of boundary in the final GBCDs of all of the GBE materials, so it seems that they must play a dominant role in the evolution of the GBCD during processing. Although there have been many reports on the enhancement of the concentration of SBs by thermomechanical processing, the factors influencing the formation of SBs and the mechanisms of GBCD evolution are not yet known.

The present work follows from the authors' earlier investigations of the GBCDs of Pb–Ca–Sn–Al alloys used in the manufacture of maintenance-free lead acid batteries [17–22]. The studies showed that the following factors influenced the GBCD: solid solution treatments, initial microstructure (including grain size, texture, distribution of twin boundaries and second phase particles introduced by ageing), the temperature and thickness reduction of rolling, and the temperature and time of the final annealing. It is important to note that because the alloys have a low melting temperature ( $320^{\circ}\text{C}$ ) and are supersaturated in Ca and Sn, they are thermodynamically unstable with respect to the precipitation of nano-scale  $\text{Pb}_3\text{Ca}$  or  $(\text{PbSn})_3\text{Ca}$  particles at the grain boundaries

\* Corresponding author. Tel.: +86 5332786835.

E-mail address: [wang.wei.guo@163.com](mailto:wang.wei.guo@163.com) (W. Wang).

and within the matrix, even at room temperature [23–26]. While this has the potential of leading to irreproducible microstructures, strict control of the processing parameters makes it possible to reproducibly synthesize materials with only negligible differences in GBCD.

Summarizing the previous work for Pb–Ca alloys, rolling with moderate strain at low temperature, followed by a short high temperature anneal is usually sufficient to produce a GBCD with a high SB content. However, a number of unresolved issues remain [22]. First, is it possible to process Pb–Ca alloys with a high SB fraction and a grain size less than 30 μm so that some strength is retained? Second, do all of the low Σ CSL (coincidence site lattice) [3] boundaries (Σ<29) influence the properties or is it only the twin related boundaries (Σ3, Σ9, Σ27)? Third, is there a maximum and/or optimal SB content that can be achieved? Finally, what are the microscopic mechanisms for change in the GBCD and how do evolving orientation relations impact special boundary formation? The purpose of the current paper is to address this final question. The evolution of the texture and GBCD has been measured after low temperature rolling and after annealing. The maximum concentration of SBs occurs when texture components with the Σ3 misorientation grow simultaneously.

## 2. Experimental descriptions

### 2.1. Sample preparation

A 25 kg cast ingot of Pb–Ca–Sn–Al alloy containing 0.08% Ca, 1.8% Sn and 0.026% Al (mass fractions) was prepared by Shanghai Flying-wheel Nonferrous Factory in China. After mechanically removing the outer layer, the ingot was forged at room temperature and a sample with the size of 400 mm × 300 mm × 200 mm was cut from the slab. The sample solutionized at 300 °C for one hour and then air cooled. Next, the sample was cold rolled with a thickness reduction of over 90% and then annealed at 270 °C for 3 min. Finally, the sample was divided into six parts.

The electron backscatter diffraction (EBSD) map of the as prepared sample, shown in Fig. 1, indicates that it has a homogenous grain size distribution with an average grain size of 10 μm and a relatively random grain orientation texture. The length fraction of Σ3 boundaries is about 25%. Other low Σ CSL boundaries make up a much smaller fraction usually less than 2% and can be neglected. This microstructure is consistent with one reported on previously by the authors [29] and suitable for the present experiment.

### 2.2. Cold rolling and annealing

The six samples were subjected to one-pass cold rolling (180 mm diameter rollers) at liquid nitrogen temperature (−196 °C) with thickness reductions of 10%, 20%, 30%, 40%, 50% and 60% and assigned reference name of 10, 20, 30, 40, 50 and 60CW, respectively (CW series of samples). Each sample was then divided into two parts; one half was kept at low temperature until the EBSD measurement while the second was annealed at 270 °C for 3 min and air cooled. The samples were sealed in Al foil prior to annealing to prevent oxidation. The annealed samples will be referred to as ANN10, ANN20, ANN30, ANN40, ANN50 and ANN60 (ANN series of samples), where the number in each name indicates the original reduction in thickness.

### 2.3. EBSD measurements

EBSD mapping was carried out in a FEI-200 Sirion field emission electron scanning microscope (FESEM) coupled with an HKL-

Channel-5 EBSD system. To prepare the samples for EBSD mapping, they were electro-chemically polished in a solution of perchloric acid:glacial acid=2:8 (volume fraction) at 30V for 10 s. All measurements were made using a sample inclination of 70°, an accelerating voltage of 20 kV, and a beam current of 50 nA. A 0.4 μm step size was used for the cold rolled samples and a 5.0 μm step size was used for the annealed samples. Areas of 1000 μm by 800 μm were mapped. For the cold rolled samples, more than 80% of the points were indexed correctly and, for the annealed samples, more than 90% of the points were indexed correctly.

### 2.4. Data processing

HKL-Channel-5 software was used to remove poorly indexed points, calculate misorientation distributions functions (MDFs), and determine special boundary fractions. For the misorientation distribution functions, the axis angle convention was used and 1° of misorientation was taken as the lower limit. The SB fractions were calculated with both the Brandon [30] and Aust–Palumbo [31] criteria and are specified as length fractions.

Orientation distribution functions (ODFs) were calculated from the EBSD measurements using the Gaussian Kernel Estimation method. In the calculation, it was assumed that the pole intensity in one orientation in Euler space can be expressed as a Gaussian function as

$$I(\psi) = I_0 \exp \left[ - \left( \frac{\psi}{\psi_0} \right)^2 \right] \quad (1)$$

where  $\psi_0$  is the half width of Gaussian peak usually takes 5°,  $\psi$  is the deviation angle from the center of the orientation and  $I_0$  is the maximum pole intensity at the center of the orientation and can be determined experimentally as [32]

$$I_0 = \exp \left( \frac{\left( \sum_{i=1}^n \psi_i^2 \right) \left( \sum_{i=1}^n \psi_i^2 \ln I_i \right) - \left( \sum_{i=1}^n \ln I_i \right) \left( \sum_{i=1}^n \psi_i^4 \right)}{\left( \sum_{i=1}^n \psi_i^2 \right)^2 - n \sum_{i=1}^n \psi_i^4} \right) \quad (2)$$

where  $\psi_i$  is the deviation angle from the center of the concerned orientation and  $I_i$  the corresponding measured intensity, and  $n$  is the number of measurements. The cut-off for  $\psi_i$  was two times the half width  $\psi_0$ . The cell size (clustering) of the divided Euler space and the resolution was specified by 5° and 16 × 16 × 16, respectively. The texture components were determined by comparing the ODF results with the standard orientations and those that deviated from the standard orientations were ascertained by Tex-Tools according to their Euler angles.

Because the majority of special boundaries in GBE materials are Σ3 type, we further analyzed the distribution of grain boundary plane orientations of these boundaries. A previously described stereological method [27,28] was used for these calculations. Grain boundary line segments were first extracted from the maps using TSL-OIM-4.3 software [33,34]. These segments were analyzed in two ways. First, the line segment direction for all Σ3 grain boundaries was compared to the ideal direction for a coherent twin. The observed segment orientation was less than 10° from the ideal orientation, it was classified as a coherent twin. If not, it was classified as an incoherent twin. Second, the stereologically determined grain boundary plane distribution  $\lambda(60^\circ/[111]n)$ , in the bicrystal reference frame, was computed. The results are presented on a stereographic projection in units of multiples of a random distribution (MRD).

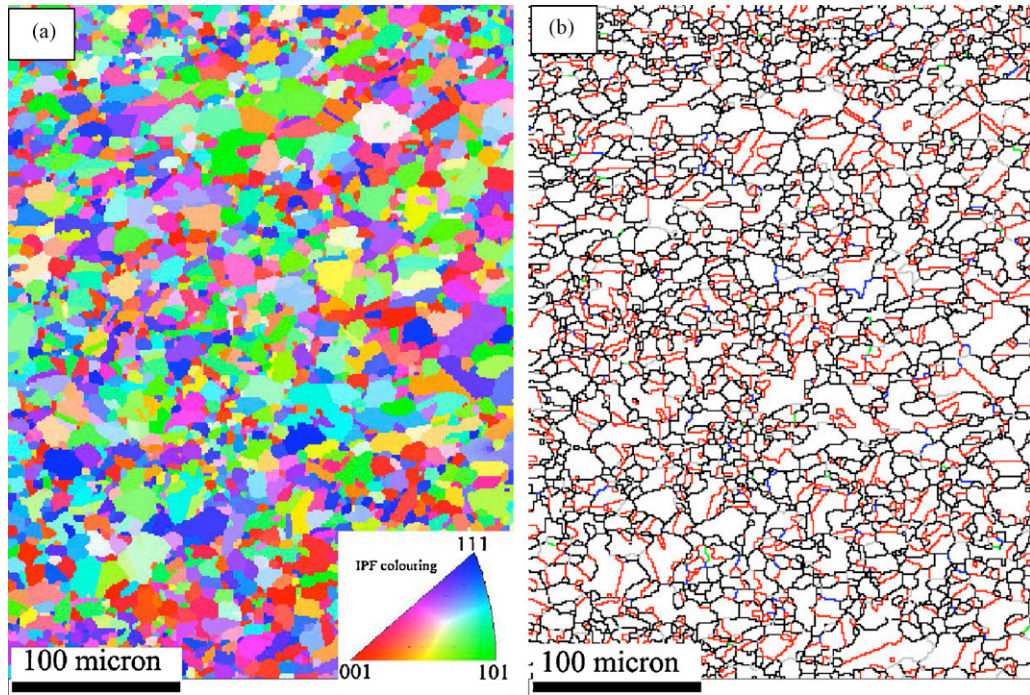


**Fig. 1.** EBSD microstructures of the sample as prepared. (a) The orientation imaging microscopy (OIM); (b) GBCDs of the same area in which red, blue, green and gray lines denote  $\Sigma 3$ ,  $\Sigma 9$ ,  $\Sigma 27$  and other low  $\Sigma$ CSL boundaries, respectively.

### 3. Results and discussions

#### 3.1. Textures and MDFs after cold rolled (for CW series of samples)

The  $\phi 2 = 45^\circ$  sections of ODFs are shown in Fig. 2 and the MDFs for the same samples are shown on Fig. 3. As illustrated by Fig. 2a, the 10CW sample texture had a strong single cube ( $\{001\}\{100\}$ ) component. While this is common in recrystallized fcc metals [35], we assume that a different mechanism is responsible in the lightly deformed material. According to Schmid's law, grains oriented around  $\{111\}$ //ND or  $\{110\}$ //ND are harder than those oriented near  $\{001\}$ //ND. Therefore, they might be re-oriented to

$\{001\}$ //ND by the so-called lattice rotation due to the high friction  $\sigma_{13}$  [36] between the contacted surfaces of roller and the sample during low strain cold rolling without lubrication. The origin of this cube texture, and whether it extends below the surface region, is not clear from the present experiments.

The strong brass R1 (BR1) ( $\{111\}\{112\}$ ) texture in sample 20CW (see Fig. 2b) could be developed by mechanical twinning on the  $\{111\}$  plane and  $\langle 112 \rangle$  direction. Although mechanical twinning has never been observed in a Pb–Ca-based alloy which was cold rolled at ambient temperature, it may be the most active deformation mechanism at liquid nitrogen temperature. As Paul et al. [37] observed in the study of the

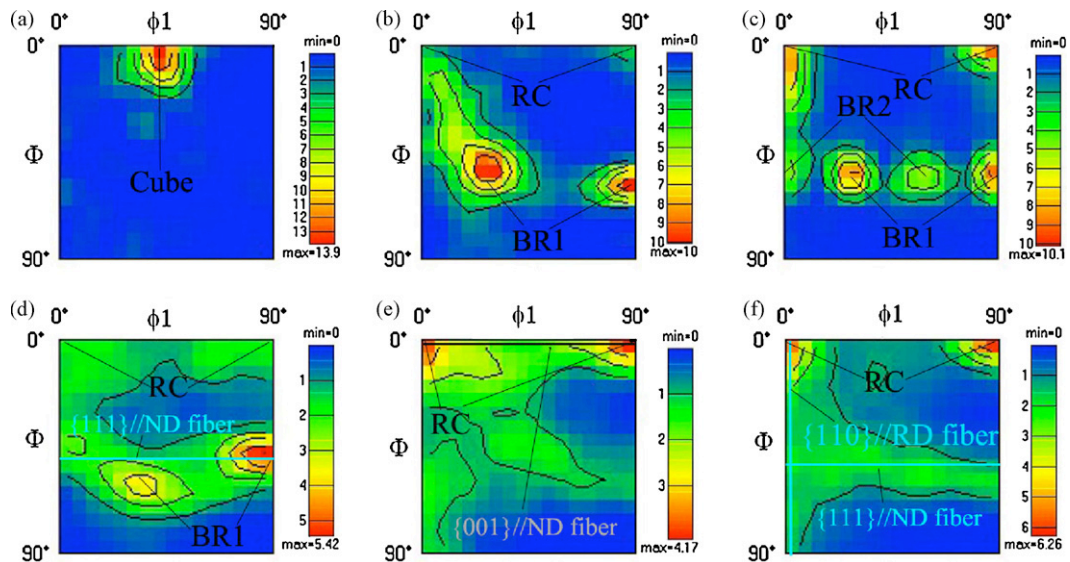


**Fig. 2.**  $\phi 2 = 45^\circ$  sections of orientation distribution functions (ODFs) of the samples of CW series. (a)–(f) Correspond to the samples 10, 20, 30, 40, 50 and 60CW, respectively. Words or characters inside the figures represent the components of textures as Cube:  $\{001\}\{100\}$ ; RC: rotated cube  $\{001\}\{110\}$ ; BR1: brass R1  $\{111\}\{112\}$ ; BR2: brass R2  $\{111\}\{110\}$ .

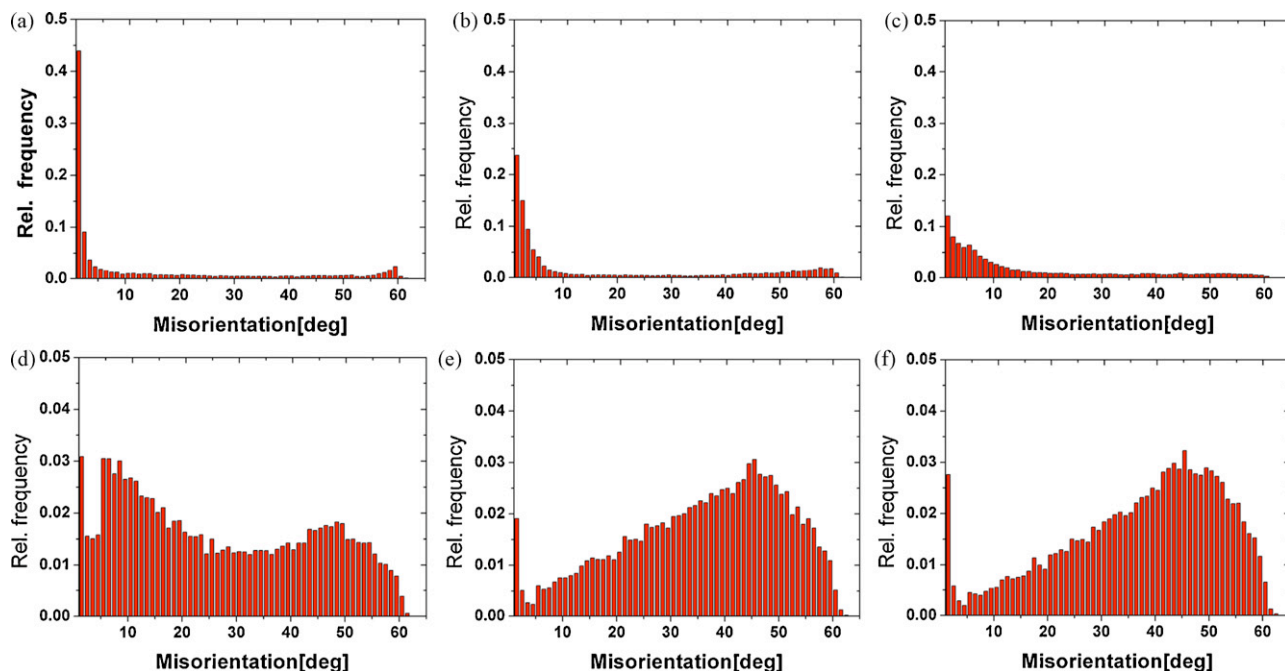


Fig. 3. Misorientation distribution functions (MDFs) of the cold rolled samples (a)–(f) correspond to the sample 10, 20, 30, 40, 50 and 60CW, respectively.

deformation behavior of C ( $\{112\}\{111\}$ ) oriented single crystal silver, such twinning usually forms a structure of very fine twin-matrix layers with an orientation of  $\{111\}\{112\}$ . Unfortunately, these structural details of the Pb–Ca-based alloys could not be revealed by EBSD mapping on the normal plane ( $TD \times RD$ ). Apart from strong BR1 texture in sample 20CW, there also appeared a weak rotated cube texture (RC) ( $\{001\}\{110\}$ ). This texture was probably produced by  $\{001\}\{110\}$  slip. Although the most active slip system in fcc metals is  $\{111\}\{110\}$ , it may be replaced by  $\{001\}\{110\}$  in Pb–Ca-based alloys at liquid nitrogen temperature.

Sample 30CW exhibited a dominant BR1 texture, a strong RC ( $\{001\}\{110\}$ ) component, and weaker brass R2 (BR2) ( $\{111\}\{110\}$ ) component (see Fig. 2c). As mentioned above, RC texture might be introduced by  $\{001\}\{110\}$  slip. The BR2 component can be attributed to the operation of  $\{111\}\{110\}$  slip, activated by the increased deformation. The fact that the intensity of the RC texture is greater than that of BR2 indicates that the  $\{001\}\{110\}$  slip system is more active than the  $\{111\}\{110\}$  system during low temperature deformation of Pb–Ca-based alloys.

A  $\{111\}$ //ND fiber texture emerged in sample 40CW (see Fig. 2d). This was introduced by the spreading of both BR1 and BR2 components required to accommodate the metal flow at 40% strain. The RC texture was also broadened so that a  $\{001\}$ //ND fiber texture was nearly formed. At this stage, the broadening of the texture peaks indicate that the sample underwent a very complicated mode of deformation in which multiple slip and shear banding [37] were activated.

The larger strains led to a spreading of the peaks in the ODFs of 50 and 60CW. Sample 50CW has a weak  $\{001\}$ //ND fiber texture (see Fig. 2e) and sample 60CW has weak  $\{111\}$ //ND and  $\{110\}$ //RD fibers (See Fig. 2f). However, compared to 40CW, the intensity of the RC texture increased with increasing strain. This phenomenon must be caused by the dynamic recrystallization [38] during rolling. Because of the material's low melting point, heat generation by rolling have initiated recrystallization. The fine equiaxed microstructure evident in the EBSD maps (see Fig. 4) and the nearly random MDFs (see Fig. 3e and f) both suggest that recrystallization occurred.

Table 1

The summary of the textures developed in the cold rolled samples (CW series of samples).

Sample	Processing treatments	Textures	Intensities
10CW	Cold rolled by 10%	Cube: $\{001\}\{100\}$	~14
20CW	Cold rolled by 20%	Brass R1 (BR1): $\{111\}\{112\}$ Rotated cube (RC): $\{001\}\{110\}$	9–10 2–3
30CW	Cold rolled by 30%	Rotated cube (RC): $\{001\}\{110\}$ Brass R1 (BR1): $\{111\}\{112\}$ Brass R2 (BR2): $\{111\}\{110\}$	8–9 8–9 5–6
40CW	Cold rolled by 40%	Brass R1 (BR1): $\{111\}\{112\}$ $\{111\}$ //ND fiber Rotated cube (RC): $\{001\}\{110\}$	~5 2–3 2–3
50CW	Cold rolled by 50%	Rotated cube (RC): $\{001\}\{110\}$ $\{001\}$ //ND fiber	3–4 1–2
60CW	Cold rolled by 60%	Rotated cube (RC): $\{001\}\{110\}$ $\{111\}$ //ND fiber $\{110\}$ //RD fiber	5–6 1–2 1–2

The texture results are summarized in Table 1. Several trends are evident. The first is that at low strains, the number of texture components increases with increasing strain. The second is that at higher strains fiber textures develop with relatively weaker texture.

There is also a clear evolution in the misorientation distributions (see Fig. 3). With increasing strain, the peak in the MDFs from the low angle range to the high angle range. (Note that the scale of relative frequency for Fig. 3a–c is 0.5 while it is 0.05 for Fig. 3d–f.) These results indicate that the deformation substructures were changing with increasing cold rolling strain. As mentioned above, the appearance of MDFs that are similar to the random distribution at the highest strain levels suggest that some recrystallization have occurred.

### 3.2. Textures and GBCDs after cold rolled and annealed (for ANN series of samples)

The ODFs of the ANN series of samples are shown in Figs. 5 and 6 and the fractions of special boundaries are listed

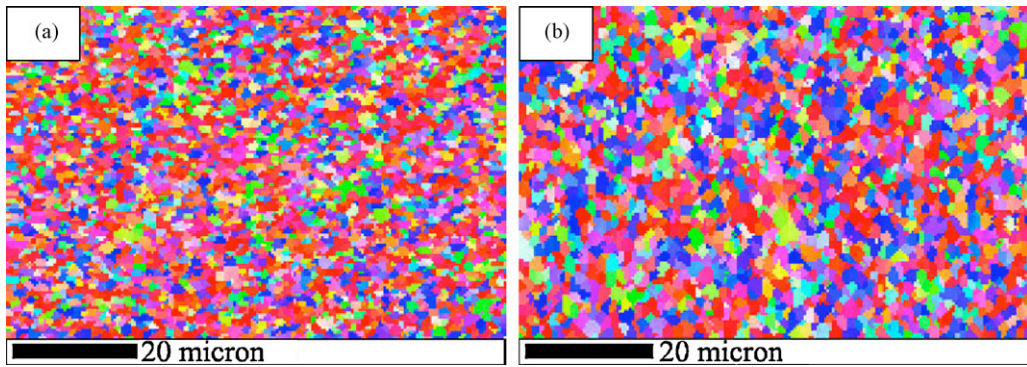


Fig. 4. Orientation imaging microscopy (OIM) of the sample 50CW (a) and 60CW (b).

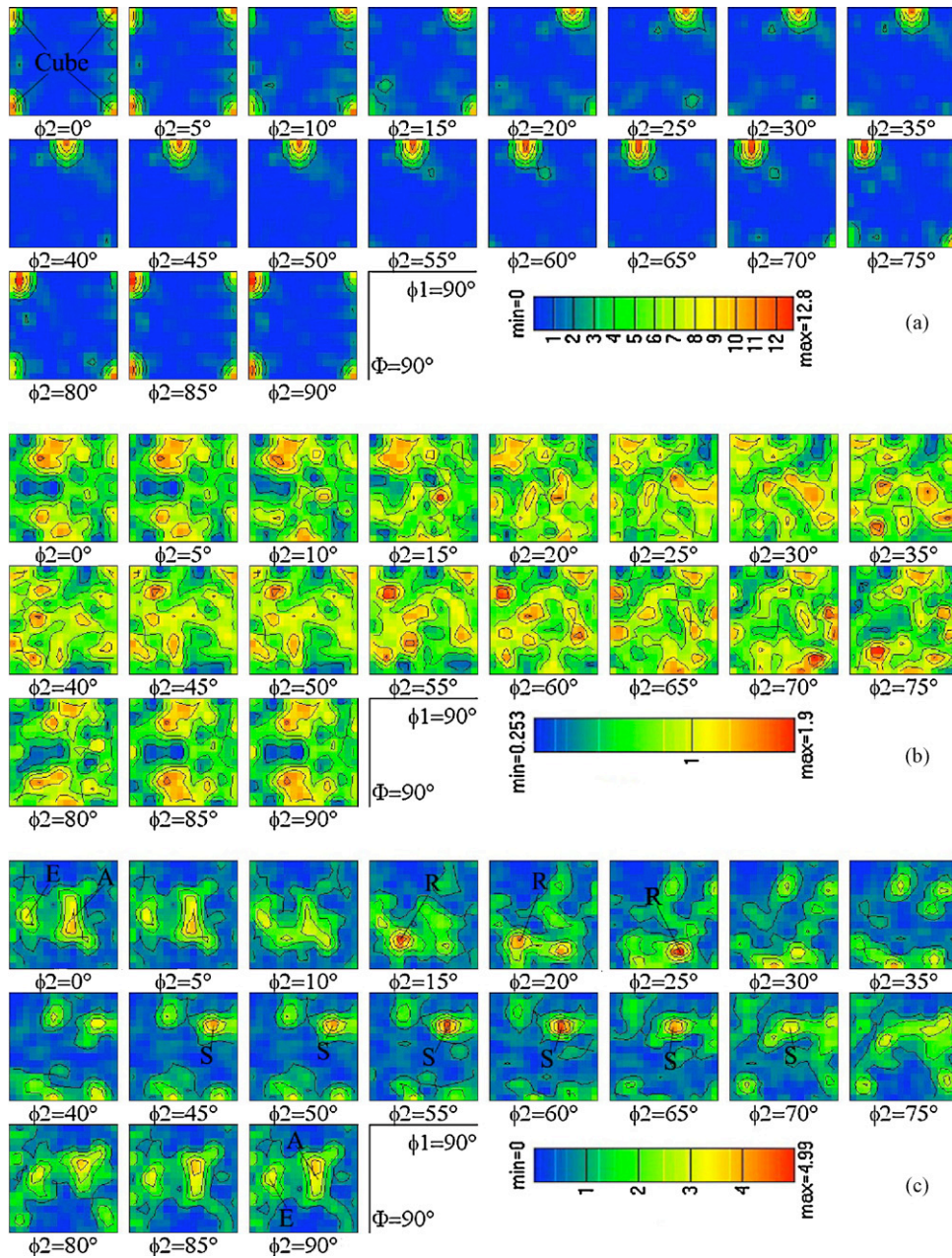
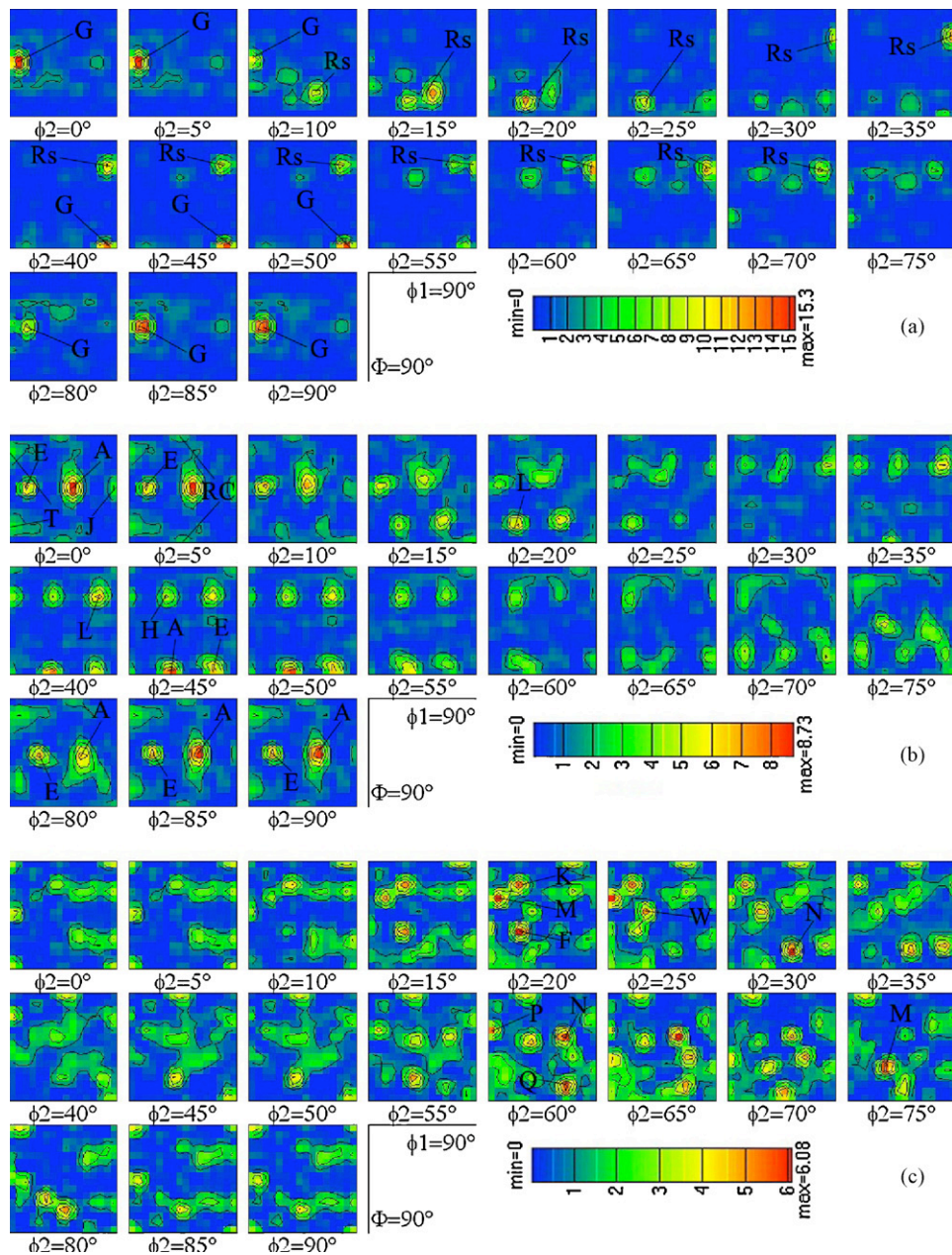


Fig. 5. Series sections of ODFs for the samples ANN10 (a), ANN20 (b) and ANN30 (c). Words or character in the figures denote the components of textures as Cube:  $\{001\}\{100\}$ ; A:  $\{110\}\{111\}$ ; E:  $\{110\}\{114\}$ ; R:  $\{124\}\{112\}$ ; S:  $\{123\}\{634\}$ .



**Fig. 6.** Series sections of ODFs for the samples ANN40 (a), ANN50 (b) and ANN60 (c). Words or character in the figures denote the components of textures as G:  $\{110\}\langle 001\rangle$ ; Rs: (R1–R7, to see table 3); T:  $\{014\}\langle 100\rangle$ ; E:  $\{110\}\langle 114\rangle$ ; A:  $\{110\}\langle 111\rangle$ ; J:  $\{110\}\langle 011\rangle$ ; RC:  $\{001\}\langle 110\rangle$ ; L:  $\{113\}\langle 112\rangle$ ; H:  $\{113\}\langle 114\rangle$ ; K:  $\{125\}\langle 551\rangle$ ; M:  $\{124\}\langle 210\rangle$ ; F:  $\{123\}\langle 112\rangle$ ; N:  $\{123\}\langle 412\rangle$ ; P:  $\{123\}\langle 120\rangle$ ; Q:  $\{210\}\langle 125\rangle$ ; W:  $\{122\}\langle 212\rangle$ .

in Table 2. Although all of the samples were annealed the same way after cold rolling, the textures and GBCDs are quite different due to the different microstructures formed before annealing.

In sample ANN10, a very strong cube texture (Fig. 5a) was inherited from the deformation texture in sample 10CW (Fig. 2a). In this case, SBs fraction (Table 2) reduced from 30% in the initial sample to 13% (excluding  $\sum 1$ s because they are usually the sub-grain

**Table 2**  
Measurement results of GBCDs of the cold rolled and annealed samples (ANN series).

Sample	Brandon criterion						Aust-Palumbo Criterion					
	$\sum 1$ (%)	$\sum 3$ (%)	$\sum 9$ (%)	$\sum 27$ (%)	Other SBs (%)	Total SBs (%)	$\sum 1$ (%)	$\sum 3$ (%)	$\sum 9$ (%)	$\sum 27$ (%)	Other SBs (%)	Total SBs (%)
ANN10	33.0	9.3	0.8	0.2	2.7	13.0	33.0	7.4	0.3	0.1	0.3	8.1
ANN20	2.6	28.5	7.0	2.9	2.8	41.2	2.0	27.1	6.5	2.1	0.3	36.0
ANN30	1.0	42.7	11.0	4.0	1.7	59.4	1.0	41.8	10.7	2.9	0.0	55.4
ANN40	1.0	54.7	16.7	8.4	1.0	80.8	1.0	53.5	16.7	5.9	0.0	76.1
ANN50	1.0	56.8	12.7	7.2	0.8	77.5	1.0	55.9	12.6	5.6	0.0	74.1
ANN60	2.0	48.4	10.9	4.8	1.8	65.9	2.0	47.6	10.5	3.5	0.0	61.6

**Table 3**  
Summary of the grain orientations as marked in Figs. 10a and 11a.

Figures	Markers	Euler angles ( $\phi_1, \Phi, \phi_2$ ) $^\circ$	Orientations ( $hkl$ )[ $uvw$ ]
10a	G1	(192, 45, 88)	(101)[010]
	G2	(80, 44, 1)	(011)[1-44]
	R2	(275, 21, 45)	(114)[22-1]
	R4	(108, 23, 30)	(125)[-4-32]
	R5	(223, 20, 62)	(216)[14-1]
	R6	(75, 19, 30)	(126)[-2-83]
	R7	(134, 24, 37)	(237)[-9-13]
11a	R1	(275, 26, 28)	(124)[21-1]
	R3	(35, 31, 60)	(213)[0-31]
	Gv	(174, 38, 82)	(203)[010]

boundaries and do not constitute the real parts of the GB networks), indicating that low-strain cold rolling followed by high temperature annealing had a negative effect on the SB concentration. Sample ANN20 (Fig. 5b) has very weak texture. The relatively strong BR1 texture after cold rolling has been randomized; this must be caused by continuous recrystallization (CR) [38] which leads to a microstructure that is similar to the starting structure prior to cold rolling. The GBCD is also similar to the original specimen. The percentage of  $\Sigma 3$  in ANN20 is 28%, very near the concentration in the initial sample (25%). The higher fraction of  $\Sigma 9 + \Sigma 27$  SBs in sample ANN20 must be generated by the interactions of mobile incoherent  $\Sigma 3$  [39] boundaries formed by the distortion of twins during cold rolling [29].

As shown in Fig. 5c, ANN30 developed texture mainly with S ( $\{123\}\{634\}$ ) and R ( $\{124\}\{112\}$ ) components, but also weak A ( $\{110\}\{111\}$ ) and E ( $\{110\}\{114\}$ ) components. Note that the rolling texture has been completely replaced and the GBCD has also changed dramatically. The SB fraction in ANN30 is close to 60%, which is twice the initial concentration. Sample ANN40 underwent a similar transformation in which its texture after cold rolling was completely replaced by strong Gauss or ( $\{110\}\{001\}$ ) and Rs (R1–R7, to see Table 3) components (Fig. 6a). It is interesting to note that in all of the R components, the orientations of the crystal planes parallel to the sample normal plane all lie within a  $17^\circ$  range between  $\{114\}$  and  $\{123\}$ . Furthermore, the special boundary content in this sample reached a maximum (81%) and the connection between this and the texture will be discussed further in Section 3.3. Sample ANN50 and ANN60 developed a range of texture components that are best described by an A ( $\{110\}\{111\}$ ) component, a weaker E ( $\{110\}\{114\}$ ), and an L ( $\{113\}\{121\}$ ) component (see Fig. 6b and c). Note that the L component can be categorized with the Rs textures as shown in Figs. 10 and 11a and Table 3. The SB fraction of 77% in sample ANN50 is also relatively high.

The data in Table 2 show that more than 95% SBs are the  $\Sigma 3^n$  ( $n=1, 2, 3$ ) types, regardless of the criteria used. This is consistent with previous reports from other fcc metals [40–43] with low to medium stacking fault energy. Assuming that the formation of  $\Sigma 9$  and  $\Sigma 27$  boundaries is dominated by  $\Sigma 3$  boundaries [17], then the ratio of boundary fraction between ( $\Sigma 9 + \Sigma 27$ ) and  $\Sigma 3$  should be a significant parameter [29]. This ratio, referred to as the ‘R value’ reflects the ability of  $\Sigma 3$  boundaries, per length, to produce  $\Sigma 9$  and  $\Sigma 27$  boundaries. Table 2 and Fig. 7 show that the R value is maximized for the ANN40 sample. The SB fractions given in Table 2 show a similar trend, also reaching a maximum for the ANN40 sample. So, it seems reasonable that a well optimized GBCD should contain both higher fraction SBs and higher fraction  $\Sigma 9 + \Sigma 27$  boundaries.

Fig. 8 shows the spatial distribution of grain boundaries with different characters. The images clearly illustrate the same variations in the SB fraction that are listed in Table 2. The other notable features in the micrograph are the sizes of the clusters of grains with  $\Sigma 3^n$  relationships (referred to as  $\Sigma 3^n$  CG) [44] and loca-

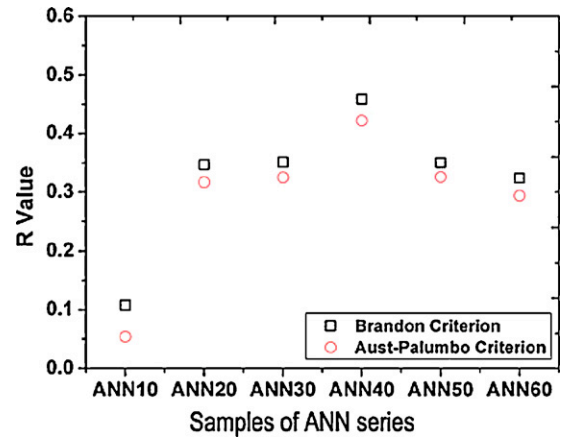


Fig. 7. R values of the samples of ANN series.

tions where the connectivity of random high angle grain boundary (HABs) networks are interrupted. The cluster size increases from less than  $50 \mu\text{m}$  in the ANN20 sample to greater than  $400 \mu\text{m}$  in ANN40. In Fig. 8d, there are many small grains within the cluster labeled C that are bounded by  $\Sigma 3^n$  ( $n=1, 2, 3$ ) boundaries (the thin gray lines). Because most  $\Sigma 3^n$  ( $n=1, 2, 3$ ) SBs are corrosion resistant [1], the coarsening of the  $\Sigma 3^n$  CG size imparts the intergranular corrosion resistance of coarse microstructures in materials with much smaller average grain sizes. The locations where the grain boundary network is interrupted (labeled X, Y, and Z in Fig. 8d) are also positions where intergranular corrosion cracking may be blocked by corrosion resistant special boundaries. So, high fractions of SBs, larger sizes of  $\Sigma 3^n$  CG (while preserving a relatively small average grain size), and more interruptions of the HABs networks all occur in the ANN40 sample and are expected to lead to improved corrosion resistance.

In brief, the results show that because samples with rolling strains less than 30% exhibit strong cube or BR1 textures, and those with strains greater than 50% undergo dynamic recrystallization, they do not lead to samples with high SB fractions or large  $\Sigma 3^n$  CG sizes. The sample with 40% strain had the best combination of characteristics. It is believed that the 40% cold work, which was at the transition between deformation and dynamic recrystallization, led to the formation of the G and Rs textures and these components are ultimately responsible for the high content of SBs. This point is discussed further in the next section.

### 3.3. Mechanism for the formation of high special boundary concentrations

Fig. 9a shows the orientation map of sample ANN40. We can see that nearly two thirds of the area is colored green (G-oriented grains and their variants) and pink or light red (Rs-oriented grains). This is consistent with the ODF results shown in Fig. 6a. As a supplement to Fig. 8d, Fig. 9b shows the SB distribution which enables a detailed comparison between the orientation map and the boundary types. The area labeled A in Fig. 9a is magnified in Fig. 10a and the grain orientations marked as G1, G2, R2, R4, R5, R6 and R7 are specified by both  $\{111\}$  pole figures (Figs. 10b–h) and the Euler angles (Table 3). Although it was impossible for us to carry out in situ observations of the microstructure evolution using EBSD, Fig. 10a shows a clear growth front of high angle boundaries, marked by bold arrows, behind which are grains with strong G (or G1(101)[010]) and R2 ((114)[22-1]) textures. Such a microstructure typically arises from so-called oriented growth (OG) [45]. The matrix  $M_{R2-G}$

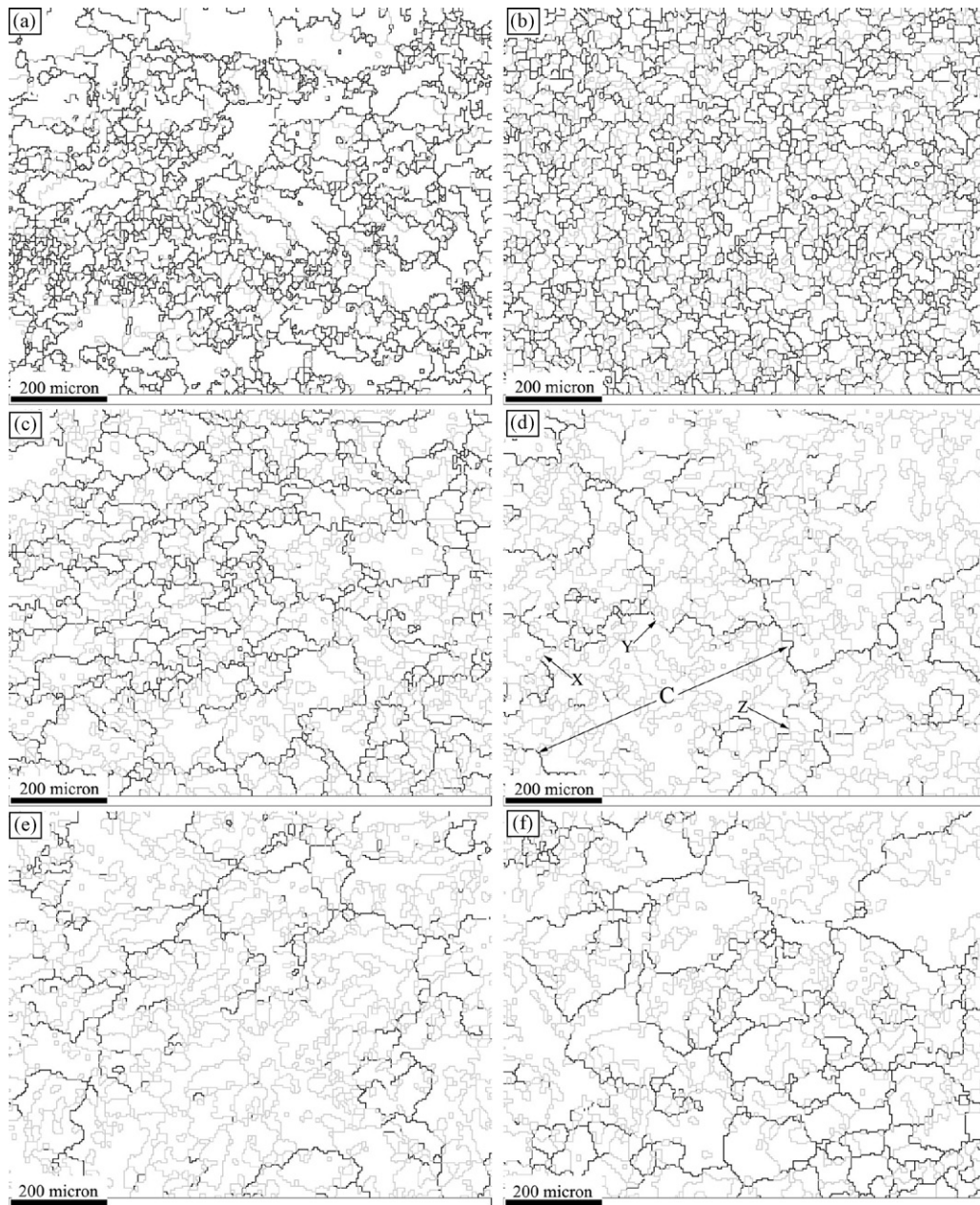


**Fig. 8.** EBSD-reconstructed grain boundary distributions for the samples of ANN series. (a)–(f) corresponds to sample ANN10, ANN20, ANN30, ANN40, ANN50 and ANN60, respectively. Black and gray lines denote the random high angle boundaries (HABs) and low  $\Sigma$  ( $1 < \Sigma < 29$ ) CSL boundaries (special boundaries or SBs). Brandon criterion was used in assessing the boundary characters.

of misorientation between G and R2 orientations is: [46]

$$M_{R2-G} = M_{R2} M_G^{-1} = \begin{bmatrix} 2 & -9 & 1 \\ 2 & 9 & 1 \\ -1 & 0 & 4 \end{bmatrix} \begin{bmatrix} 0 & 1 & 0 \\ -0.5 & 0 & 0.5 \\ 0.5 & 0 & 0.5 \end{bmatrix} = \begin{bmatrix} 5 & 2 & -4 \\ -4 & 2 & 5 \\ 2 & -1 & 2 \end{bmatrix} \quad (3)$$

According to Eq. (3), the misorientation between the G1 and R2 orientations is, in axis angle terms, a  $60^\circ$  rotation about (1 1 1), also known as  $\Sigma 3$ . Therefore,  $\Sigma 3$  boundaries are produced whenever G1 and R2 grains impinge during OG. Geometric variations of G1 and R2 are also apparent in Fig. 10a. For example, G2 (rotated  $70^\circ$  around [1 0 1]) forms a  $\Sigma 9$  boundary when it meets R2 grain.  $\Sigma 27$  boundaries are formed when G2 encounters certain variants of R2. For example, see the location marked O where a grain with R7 orientation meets G2. Furthermore,  $\Sigma 9$  boundaries (labeled P) and  $\Sigma 27$  boundaries (labeled Q) can form when two R2 variants meet.

Similarly, Fig. 11a shows a magnified view of the area labeled B in Fig. 9a. The orientations of grains labeled R1, R3, and Gv are specified by {1 1 1} pole figures (Figs. 11b–d) and Euler angles (Table 3). In this case, OG occurred with the grains of R1 ((1 2 4)[2 1 -1]) and  $\Sigma 3$  boundaries are produced by the contacts between R1 and R3 ((2 1 3)[0 -3 1]) grains (R3 is a variant of R1 that makes up a minority of the area). The R1 grains differ from the R2 grains in Fig. 10a in that few variants (only R3) occurred during its OG. The grains labeled Gv ((2 0 3)[0 1 0]) have an orientation very close to that

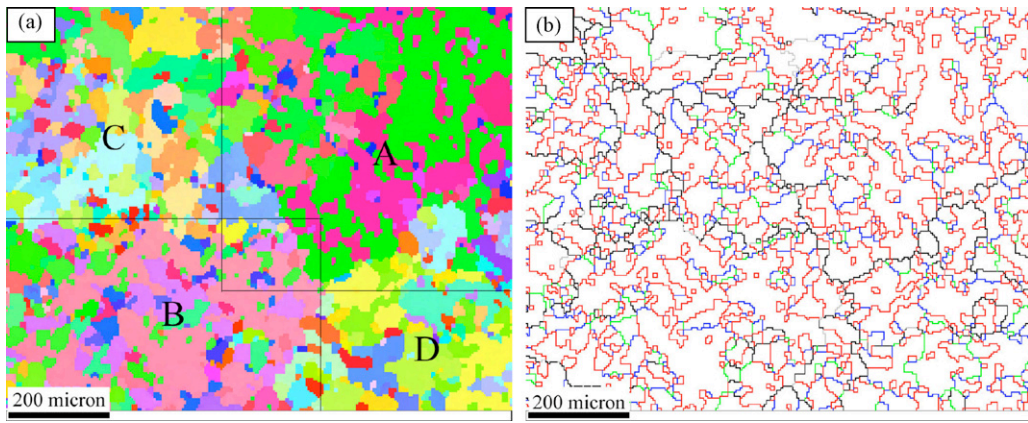


**Fig. 9.** OIMs (a) and GBCDs (b) of sample ANN40. The same meaning of coloring in (a) as that in Fig. 1a; the red, blue, green, gray and black lines in (b) denote  $\Sigma 3$ ,  $\Sigma 9$ ,  $\Sigma 27$ , other SBs and random high angle grain boundaries (HABs), respectively.

of G1 (Fig. 10a), but make up a much smaller portion of the area than R1. The circles in Fig. 11a indicate clusters of small grains that mostly have  $\Sigma 3^n$  ( $n = 1, 2, 3$ ) boundaries. There are only a few HABs (labeled H) within these clusters. The clusters appear to be trapped within the growing R1 grain, presumably because of the low mobility to the  $\Sigma 3^n$  boundaries at the periphery. These clusters not only contribute SBs to the GBCD, they also make up the network that preserves the relatively small average grain size.

The considerations above suggest that it is the misorientation relationships among the grains with G1, R2, R1 and R3 orienta-

tions during annealing that lead to the large fraction of special boundaries in the ANN40 sample. Similarly, the high concentration of special boundaries in the ANN50 sample derives from the A ( $\{110\}\{111\}$ ) and E ( $\{110\}\{114\}$ ) components, which are close to G1, and the L ( $\{113\}\{121\}$ ) component, which is close to R2.

Next, we consider how the recrystallization nuclei with the G1, R2, R1 and R3 orientations formed. Hirsch [47] and Paul [48–50] have observed that when single crystal Cu and Cu-2%Al are deformed at liquid nitrogen temperature, two main groups of texture components develop; for twins the texture component is

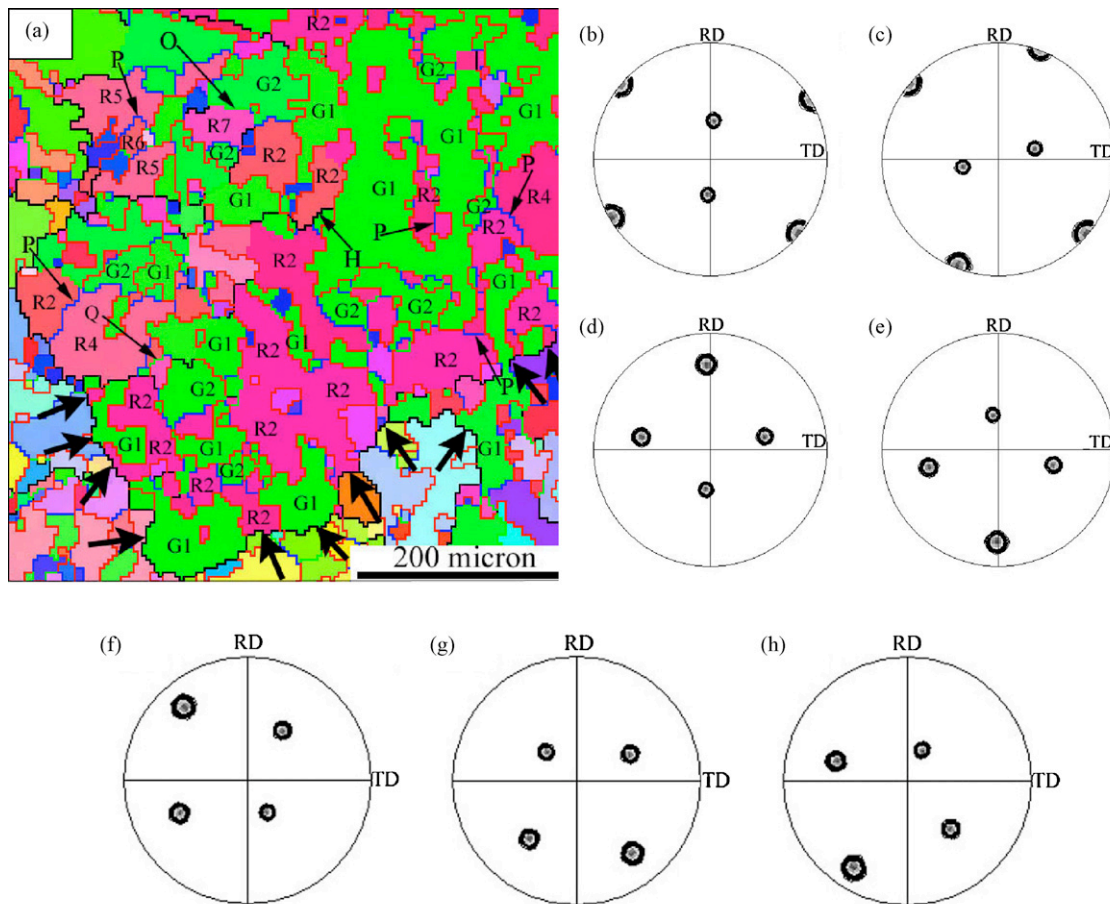


**Fig. 10.** (a) Magnified details of area A as marked in Fig. 9a in which the colored lines have same meaning as that in Fig. 9b; (b)–(h) are the  $\{111\}$  pole figures of grains in sequence G1, G2, R2, R4, R5, R6 and R7 as marked in (a).

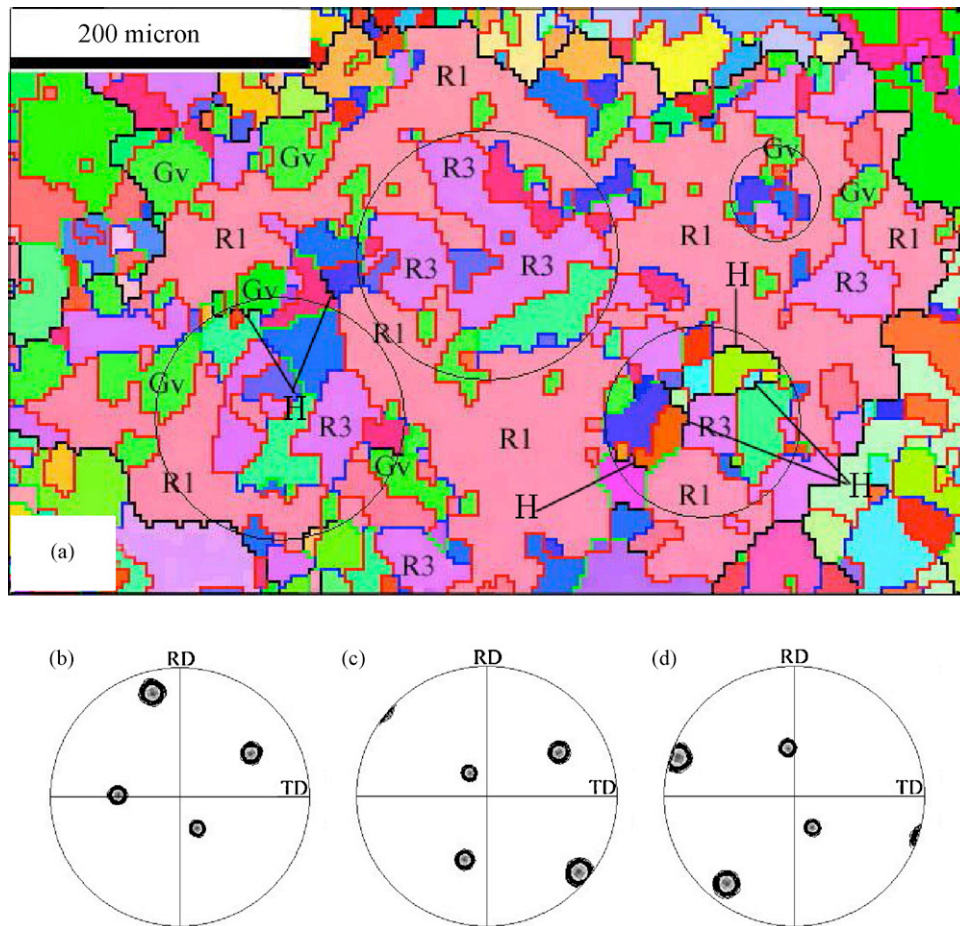


**Fig. 11.** (a) Magnified details of area B as marked in Fig. 9a in which the colored lines have same meaning as that in Fig. 9b; (b)–(d) are the  $\{111\}$  pole figures of grains in sequence R1, R3 and Gv as marked in (a).

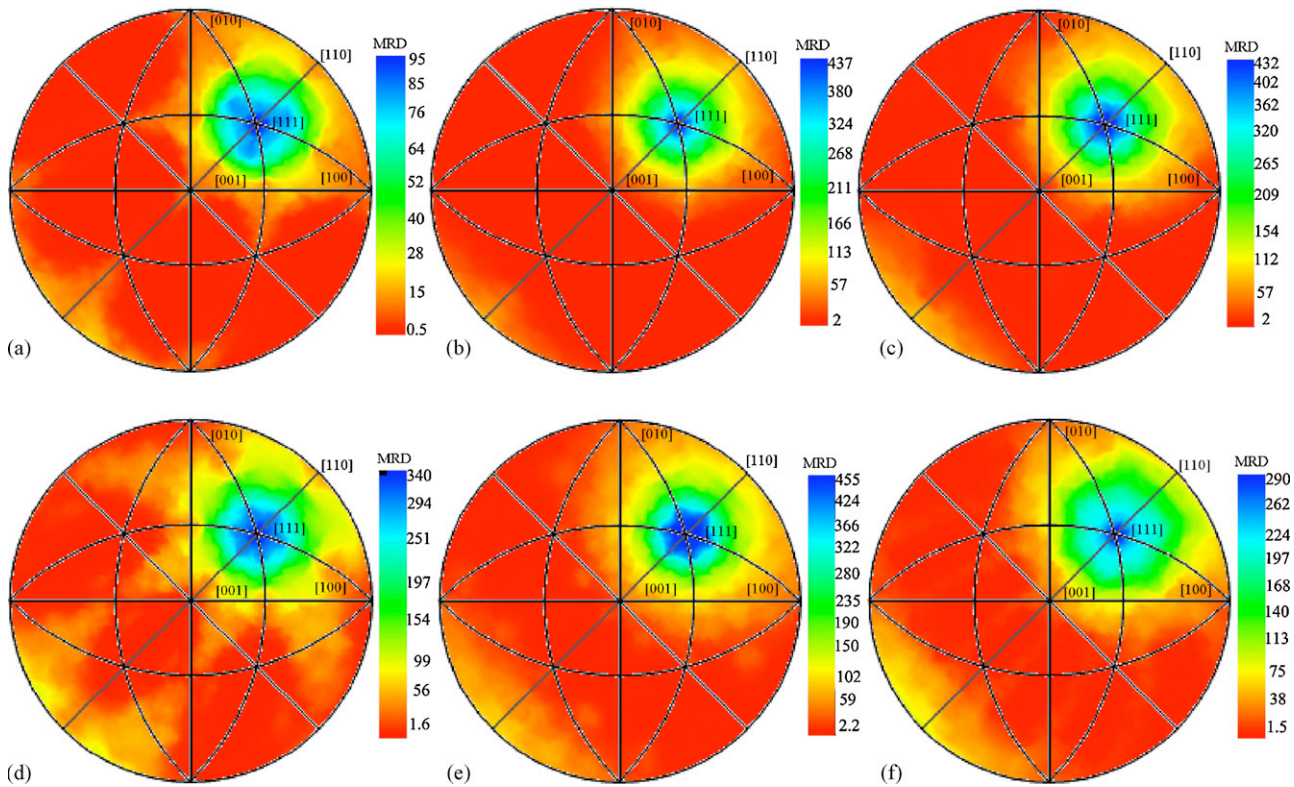
near  $G1\{110\}\langle 001\rangle$  and for the matrix it is near  $R2\{114\}\langle 221\rangle$ . Because fine-grained polycrystalline samples were used in the present work, it was reasonable that G1 and R2 texture components were not detected in the deformed samples. Some of the grains must have had orientation that were very close that that used by Paul [48–50]. So, the nuclei of the G1, R2, R1 and R3 orientations could be formed by the deformation of grains with specific orientations. The observations also suggest that the deformation texture of the 40CW sample favors the OG of these nuclei. While the G1, R2, R1, and R3 orientation emerged in ANN30, ANN40 and ANN50, they only grew extensively in ANN40. Note that in the places that were not favorable for the growth of G1 and R2 (or R1 and R3) textures, labeled C and D in Fig. 9a, the SB fraction is much lower (65%) than the average (81%).

Table 4 summarizes the characteristics of the  $\Sigma 3$  boundaries that make up the majority SBs in the GBCDs of the samples of the ANN series. Both the number and length fraction of  $\Sigma 3$  boundaries

increased from ANN10 to ANN40, and was then relatively constant for ANN50 and ANN60. This trend in the total fraction of  $\Sigma 3$  boundaries is the same as the trends in the coherent ( $\Sigma 3_c$ ) and incoherent ( $\Sigma 3_{ic}$ ) fractions. The data in Table 4 is based upon a binary classification of the data into coherent or incoherent  $\Sigma 3$  boundaries. Fig. 12 shows the complete distribution of the  $\Sigma 3$  grain boundary planes that result from the five parameter analysis. Note that the intensity of the peak at position of the coherent twin,  $[111]$ , is lowest in Fig. 12a because this sample has the fewest  $\Sigma 3$  boundaries. All of the other peaks are more than three times larger. The spreading of intensity away from the ideal  $[111]$  position is an indication of the relative number of incoherent boundaries. In particular, the distribution for ANN40 is the broadest and intensity approaching 100 MRD can be seen stretching across the entire range of plane orientations. This is consistent with the fact that this sample had the highest length fraction of incoherent boundaries (Table 4). Because a larger deviation angle from the  $[111]$  coherent position implies

**Table 4**  
Statistics of  $\Sigma 3$  boundaries in the samples of ANN series (Brandon criterion used).

Sample	Number fraction					Length fraction				
	Non- $\Sigma 3$ (%)	$\Sigma 3$ (%)	$\Sigma 3_c$ (%)	$\Sigma 3_{ic}$ (%)	$\Sigma 3_{ic}/\Sigma 3_c$	Non- $\Sigma 3$ (%)	$\Sigma 3$ (%)	$\Sigma 3_c$ (%)	$\Sigma 3_{ic}$ (%)	$\Sigma 3_{ic}/\Sigma 3_c$
ANN10	89.8	10.2	2.2	8.0	4.0	90.5	9.5	3.0	6.5	2.2
ANN20	80.2	19.8	8.2	11.6	1.4	71.7	28.3	12.8	15.5	1.2
ANN30	65.5	34.5	10.5	24.0	2.3	56.8	43.2	16.9	26.3	1.6
ANN40	52.3	47.7	12.2	35.5	2.9	44.9	55.1	16.8	38.3	2.3
ANN50	48.5	51.2	14.9	36.3	2.4	43.3	56.7	21.4	35.3	1.6
ANN60	56.6	43.4	10.4	33.0	3.2	51.2	48.8	14.7	34.1	2.3



**Fig. 12.** Complete distribution of the  $\Sigma_3$  grain boundary planes  $\lambda(60^\circ/[111]n)$  obtained by five parameter analyses (FPA). (a)–(f) correspond in sequence to the samples ANN10–ANN60.

a higher energy and higher mobility [51,52] for  $\Sigma_{3ic}$  boundaries, a higher fraction of such boundaries implies that they will interact more frequently and more  $\Sigma_9$  and  $\Sigma_{27}$  boundaries will be created. This is consistent with the resulting peak  $R$  value (0.46) observed in sample ANN40 (Fig. 7).

Finally, it should be noted that the mechanism proposed here for increasing the fraction of SBs involves the oriented growth of both G1 (Goss) and Rs (R1–R7) during annealing. This mechanism is different from that proposed by the authors elsewhere [22] which was related to strain induced boundary migration [53] and annealing twinning. This earlier mechanism produced materials with a low  $R$  value and no texture. The current mechanism is also distinct from more well-known grain boundary engineering processes which typically result in untextured materials.

#### 4. Summary and conclusions

Studies of the texture and GBCD evolution of Pb–Ca alloys, cold worked at liquid nitrogen temperature and annealed, led to the following conclusions.

Cold rolling with strains of about 40% promotes the formation of a microstructure with a special boundary fraction of 81% when the sample is annealed. This material has an  $R$  value of 0.46 and clusters of grains made up of special boundaries that are 200–400  $\mu\text{m}$  in diameter. Higher and lower strains produced microstructure with inferior characteristics.

The microstructure with the highest special boundary fraction resulted from a cold rolled texture that includes a BR1 component, a weaker  $\{111\}$ /ND fiber, and scattered RC components.

The mechanism of special boundary formation involves the oriented growth of Goss and Rs (R1–R3) orientations during the annealing. Because the orientation relationship between Goss and R2 (and any two of their geometric variants) creates  $\Sigma_3^n$  ( $n = 1, 2,$

3) misorientations, the fraction of these boundaries increases when oriented growth occurs during annealing.

#### Acknowledgements

This work was supported by the Nature Science Foundation of China (NSFC) under the contract No. 50771060. GSR acknowledges support from the MRSEC program of the NSF under Award DMR-0520425.

#### References

- [1] G. Palumbo, U. Erb, *MRS Bull.* 11 (1999) 27.
- [2] E.M. Lehockey, G. Palumbo, P. Lin, A. Brennenstuhl, *Metall. Mater. Trans.* 29A (1997) 387.
- [3] T. Watanabe, *Res. Mech.* 11 (1984) 47–84.
- [4] M.L. Kronberg, F.H. Wilson, *Trans. AIME* 185 (1949) 501.
- [5] D.S. Lee, H.S. Ryoo, S.K. Hwang, *Mater. Sci. Eng.* 354A (2003) 106.
- [6] M. Shimada, H. Kokawa, Z.J. Wang, Y.S. Sato, I. Karibe, *Acta Mater.* 50 (2002) 2331.
- [7] M. Michiuchi, H. Kokawa, Z.J. Wang, Y.S. Sato, K. Sakai, *Acta Mater.* 54 (2006) 5179.
- [8] S. Raghuvir, G.C. Sandip, B.R. Kumar, S.K. Das, P.K. De, I. Chatteraj, *Scripta Mater.* 57 (2007) 185.
- [9] B.R. Kumar, S.K. Das, B. Mahato, A. Das, S.G. Chowdhury, *Mater. Sci. Eng. A* 454–455 (2007) 239.
- [10] X.Y. Fang, K. Zhang, H. Guo, W.G. Wang, B.X. Zhou, *Mater. Sci. Eng. A* 487 (2008) 7.
- [11] M. Kumar, A.J. Schwartz, W.E. King, *Acta Mater.* 50 (2002) 2599.
- [12] B. Alexandreanu, B. Capell, G.S. Was, *Mater. Sci. Eng. A* 300 (2001) 94.
- [13] B. Alexandreanu, B.H. Sencer, V. Thaveprungsriporn, G.S. Was, *Acta Mater.* 51 (2003) 3831.
- [14] S. Xia, B.X. Zhou, W.J. Chen, W.G. Wang, *Scripta Mater.* 54 (2006) 2019.
- [15] H. Davies, V. Randle, *Phil. Mag.* A 81 (2001) 2553.
- [16] S.Y. Lee, Y.B. Chun, J.W. Han, S.K. Huang, *Mater. Sci. Eng. A* 363 (2003) 307.
- [17] W.G. Wang, B.X. Zhou, L. Feng, *Acta Metall. Sinica* 42 (2006) 715.
- [18] S. Xia, B.X. Zhou, W.J. Chen, W.G. Wang, *Acta Metall. Sinica* 42 (2006) 129.
- [19] X. Zhang, W.G. Wang, H. Guo, Y. Jiang, *Acta Metall. Sinica* 43 (2007) 454.
- [20] K. Zhang, W.G. Wang, X.Y. Fang, H. Guo, *Acta Metall. Sinica* 44 (2008) 652.
- [21] W.G. Wang, H. Guo, *Mater. Sci. Eng. A* 445–446A (2007) 155.
- [22] W.G. Wang, F.X. Yin, H. Guo, H. Li, B.X. Zhou, *Mater. Sci. Eng. A* 491 (2008) 199.

- [23] J.P. Hilger, J. Power Sources 72 (1998) 184.
- [24] R.D. Prengaman, J. Power Sources 95 (2001) 224.
- [25] A. Matre, G. Bourguignon, J.M. Fiorani, J. Ghanbaja, J. Steinmetz, Mater. Sci. Eng. A 358 (2003) 233.
- [26] A. Matre, G. Bourguignon, J.M. Fiorani, J. Steinmetz, J. Ghanbaja, P. Lailler, Mater. Sci. Eng. A 340 (2003) 103.
- [27] G.S. Rohrer, D.M. Saylor, B.S.E. Dasher, B.L. Adams, Z. Metall. 95 (2004) 197.
- [28] D.M. Saylor, B.S.E. Dasher, B.L. Adams, Metall. Mater. Trans. A 35 (2004) 1981.
- [29] W.G. Wang, B.X. Zhou, H. Guo, Mater. Sci. Forum 638–642 (2010) 2864.
- [30] D.G. Brandon, Acta Metall. 14 (1964) 1479.
- [31] G. Palumbo, K.T. Aust, E.M. Lehockey, U. Erb, P. Lin, Scripta Mater. 38 (1998) 1685.
- [32] W.M. Mao, P. Yang, L. Chen, Principals for Texture Measurements and Analyses, Metallurgy Press, Beijing, 2008.
- [33] S.I. Wright, R.J. Larsen, J. Microscopy 205 (2002) 245.
- [34] V. Randle, Scripta Mater. 44 (2001) 2789.
- [35] S.H. Hong, D.N. Lee, Mater. Sci. Eng. A 351 (2003) 133.
- [36] H.O. Asbeck, H. Mecking, Met. Sci. Eng. 34 (1978) 111.
- [37] H. Paul, J.H. Driver, C. Maurice, A. Piatkowski, Acta Mater. 55 (2007) 575.
- [38] F.J. Humphreys, M. Hatherly, Recrystallization and Related Annealing Phenomenon, Elsevier Ltd., Oxford, 2004.
- [39] V. Randle, P. Davies, B. Hulm, Phil. Mag. A 79 (1999) 305.
- [40] D. Horton, C.B. Thomson, V. Randle, Mater. Sci. Eng. A 203 (1995) 408.
- [41] V. Randle, Acta Mater. 47 (1999) 4187.
- [42] E.M. Lehockey, Brennenstuhl, I. Thompson, Corros. Sci. 46 (2004) 2383.
- [43] C.A. Schuh, M. Kumar, W.E. King, J. Mater. Sci. 40 (2005) 847.
- [44] X.Y. Fang, W.G. Wang, Z.X. Cai, H. Guo, B.X. Zhou, Mater. Sci. Eng. A527 (2010) 1571.
- [45] B.X. Zhou, Q.X. Liu, Acta Metall. Sinica 17 (1981) 363.
- [46] V. Randle, O. Engler. Introduction to texture analysis: macrotexture, microtexture and orientation mapping. Gordon and Breach science publishers, 2000.
- [47] J. Hirsch, K. Lucke, Acta Metall. 36 (1988) 2863.
- [48] H. Paul, J.H. Driver, C. Maurice, Z. Jasienski, Acta Mater. 50 (2002) 4339.
- [49] H. Paul, J.H. Driver, C. Maurice, Z. Jasienski, Mater. Sci. Eng. A 359 (2003) 178.
- [50] H. Paul, C. Maurice, E. Bouzy, J.J. Funderberger, A. Piatkowski, Z. Jasienski, Metall. Mater. Trans. A 35 (2004) 3775.
- [51] U. Wolf, F. Ernst, T. Muschik, M.W. Finnis, Phil. Mag. A 66 (1992) 991.
- [52] Koenraad G.F. Janssens, D. Olmsted, E.A. Holm, S.M. Foiles, S.J. Plimpton, P.M. Derlet, Nature Mater. 5 (2006) 124.
- [53] Y.N. Yu, Principals of Metallic Materials Science, Beijing, Metallurgy Press, 2003.